# Detection of CSR from Blue Wave Fundus Autofluorescence Images using Deep Neural Network Based on Transfer Learning

Original Scientific Paper

**Bino Nelson**
Faculty of Engineering and Technology, University of Kerala,
Thiruvananthapuram, Kerala, India.
binonelson@gmail.com

**Haris Pandiyapallil Abdul Khadir**
Department of Electronics and Communication Engineering, College of Engineering Trivandrum,
Thiruvananthapuram, Kerala, India.
haris786pa@gmail.com

**Sheeba Odattil**
Department of Electronics and Communication Engineering, T. K. M. College of Engineering,
Kollam, Kerala, India.
shb.odattil@gmail.com

***Abstract*** *– Fluid clot below the retinal surface is the root cause of Central Serous Retinopathy (CSR), often referred to as Central Serous Chorioretinopathy (CSC). Delicate tissues that absorb sunlight and enable the brain to recognize images make up the retina. This important organ is vulnerable to damage, which could result in blindness and vision loss for the affected person. Therefore, complete visual loss may be reversed and, in some circumstances, may return to normal with early diagnosis discovery. Therefore, timely and precise CSR detection prevents serious damage to the macula and serves as a foundation for the detection of other retinal disorders. Although CSR has been detected using Blue Wave Fundus Autofluorescence (BWFA) images, developing an accurate and efficient computational system is still difficult. This paper focuses on the use of trained Convolutional Neural Networks (CNN) to implement a framework for accurate and automatic CSR recognition from BWFA images. Transfer Learning has been used in conjunction with pre-trained network architectures (VGG19) for classification. Statistical parameter evaluation has been used to investigate the effectiveness of DCNN. For VGG19, the statistic parameters evaluation revealed a classification accuracy of 97.30%, a precision of 99.56%, an F1 score of 97.25%, and a recall of 95.04% when using a BWFA image dataset collected from a local eye hospital in Cochin, Kerala, India. Identification of CSR from BWFA images is not done before. This paper illustrates how the proposed framework might be applied in clinical situations to assist physicians and clinicians in the identification of retinal diseases.*

***Keywords****: Blue Wave Fundus Autofluorescence, Central Serous Retinopathy, Deep Learning, Retinal Pathology, Macular Disease*

## 1. INTRODUCTION

The retina is located near the optic nerve at the back of the eyeball and is made up of thin layers of ocular tissues [1]. The major job of the retina is to collect light from the focal length of the lens and convert it into message signals that the brain can recognize visually. As a result, the retina is regarded as an important component of the eye and is crucial for identifying diverse nearby objects. Any abnormal or impairment to the retinal layer might cause the patient to lose their vision or have visual impairments. Blindness and visual loss may be caused by Central Serous Retinopathy (CSR), one of the diseases which impacted more people worldwide. The primary reason for CSR is the clotting of the liquid medium on the Retinal Surface Area (RSA), which adversely impairs people's eyesight [2]. To prevent visual loss, early accurate CSR detection can help with treatment choices and diagnostic methods. Several imaging modalities, including Fundus photography, Optical Coherence Tomography Angiography (OCTA), and Blue Wave Fundus Autofluorescence (BWFA), are employed for this CSR detection purpose. Among all BWFA-based methods for detecting a variety of retinal diseases, it is considered the most suitable and cutting-edge imag-

ing tool. Although the BWFA imaging method is similar to ultrasonic imaging, it has a little difference in detection. Unlike ultrasound imaging, which records an ultrasound image using sound waves, BWFA imaging uses blue light rays [3]. Employing a set of endoscopes and catheters, high-definition pictures of the RSA were generated via BWFA. In BWFA images of healthy patients and those with CSR the size of the fovea, the choroid, the Inner Limiting Membrane (ILM), and serous retinal detachment could be detected.

Thanks to the recent advancement of quantitative BWFA, Artificial Intelligence (AI) categorization of eye disorders and computer-aided illness diagnosis are now feasible. Vascular occlusions, Sickle Cell Retinopathy, Age-related Macular Degeneration (AMD), and CSR have all been investigated using quantitative BWFA analysis. Recent research has shown that supervised Machine Learning (ML) is effective for categorizing a range of activities to distinguish between normal and CSR images. Deep Learning (DL) provides a simple means of promoting the clinical application of AI classification of BWFA images. The Convolutional Neural Network (CNN) method, which was designed to mimic how the human brain interprets visual data, is normally referred to as DL [4].

To extract and analyze straightforward characteristics in the early layers and information useful in the layers of the network of the feed-forward processing of visual signals, CNNs employ millions of artificial neurons, often known as parameters. Until a CNN can be trained for a specific classification task, the network parameters need to be adjusted using millions of images. The lack of currently available images for the comparatively recent imaging modality BWFA, however, presents a challenge for the practical use of DL. DL has been proven to be implemented using a Transfer Learning (TL) approach to get around the data size restriction. TL is a technique for optimizing the weights of a pre-trained CNN by adopting some of its weights and correctly retraining parts of its layers (i.e., AI classification of retinal images). TL has been investigated in fundus photography for artery-vein segmentation, glaucoma diagnosis, and diabetic macular thinning assessment. TL has recently been investigated in BWFA for the detection of AMD, diabetic macular edema, and choroidal neovascularization.

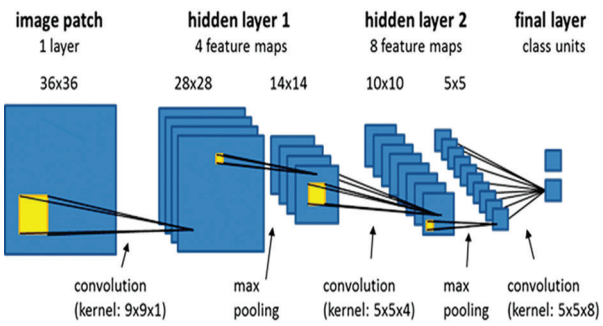


**Fig. 1.** Convolutional Neural Network for Image Classification

Because the weights in each layer can be changed, TL can theoretically entail a single layer or numerous layers. In a 16-layer CNN, for instance, the precise number of layers needed for retraining may differ based on the dataset at hand and the target job. Since there aren't as many large publicly accessible BWFA datasets, images verified by ophthalmologists have been collected from a private hospital [5]. In this study, we show how BWFA can be used for DL-based automated classification for the first time. We want to train a small dataset using TL to produce a highly accurate CSR classification.

## 2. RELATED WORKS

To evaluate CSR, Dursun et al. [6] presented the Deep Capillary Plexus (DCP-VD) and Superficial Capillary Plexus (SCP-VD) parameters. The accuracy of detection when utilizing a Support Vector Machine (SVM) is 87%. Pawan et al. [7] introduced a modified version of Capsule Network for the detection and segmentation of CSR. This algorithm is lightweight and reduces the computational overhead. While using 1792 samples this technique provides a Dice Coefficient of 94.04 and an accuracy of 91.67%. Sulzbacher et al [8] categorized neo-vascular and non-neo-vascular CSR. They utilized ML algorithms for the diagnosis of CSR. By using logistic regression, the accuracy obtained is 92.63%. Signal variations at the Chorio Capillaries (CC) level in patients with various phases were examined by Cakir et al. [9]. According to this approach, CSR patients were classified into four categories: acute, persistently atrophic, non-resolving, and inactive. CNN was used for the detection of CSR and the accuracy of detection is 92.13%. Aggarwal et al. [10] conducted an analysis to identify the differences between acute Vogt-Koyanagi-Harada disease (VKH) and acute CSR in terms of image characteristics. Sonoda et al. [11] suggested employing enhanced depth imaging to identify the anatomical changes of the choroid in eyes with CSR. The Inner and Outer Choroid structural changes technique is employed. In the images, the inner and outer choroid's hypo-reflective and hyperreflective regions were measured separately. The results revealed that the outer choroid of the CSR eyes had a significantly larger hyporeflective area (446,549 + 121,214µm2) than the control eyes (235,680 + 97,352µm2, P<0.01).

The diagnosis in CSR, according to Kulikov et al. [12], is based on ML and AI. The values for identifying subretinal fluid were 0.61, 0.99, 0.99, and 0.76, respectively, according to the analysis of test sets. For the detection of anomalies in the retinal pigment epithelium (RPE), the specificity, sensitivity, F1-score, and precision were 0.95, 0.14, 0.24, and 0.94, respectively. For leaking point identification, the sensitivity, specificity, accuracy, and F1-score were 0.06, 1.0, 1.0, and 0.12, respectively. The proposed method concluded that ML had great promise for identifying structural anomalies linked to acute CSR. Narendra et al [25] reported a CNN for the automatic segmentation of Sub-Retinal Fluid (SRF) to

identify CSR. The suggested technique, provided Dice, Recall, and Precision of 0.91, 0.83%, and 0.93%, respectively. An automatic SRF segmentation method is applied in the suggested model. Pre-processing and fluid segmentation are the two stages of the SRF segmentation method. Yoon et al. [13] proposed developing a DL system model to diagnose CSR and differentiate between chronic and acute CSR. This model's accuracy, sensitivity, and specificity for diagnosing CSR were 93.8%, 90.0%, and 99.1%, respectively. Jaisankar et al. [14] identified damaged choroidal areas and associated retinal alterations in acute and recurring CSR. Khalid et al. [15] conducted the first-ever analysis of a decision support system. The proposed system's automated disease identification is based on a multilayered SVM classifier that was trained on 40 labelled scans. With sensitivity, accuracy, and specificity ratings of 98 %, 96.92 %, and 95.86 %, respectively, the suggested approach was successfully diagnosed in 2817/2819 individuals.

Evaluation of the morphological variations in the choroidal vasculature in acute and chronic CSR was suggested by Lee et al. [16]. Different choroidal vascular dilatation patterns between acute and chronic CSR were discovered using the suggested methodology. These discoveries could aid in our understanding of the pathophysiology of CSR. In eyes with acute CSR that had not yet received treatment, Yang et al. [17] recommended using CNN to evaluate the three-dimensional choroidal vascularity index (CVI). This technique makes use of 3D-CVI, which volumetrically evaluates the choroidal vasculature, and is a valuable imaging marker of choroidal disorders, according to the suggested method, which may help better understand the pathophysiology of CSR.

In the evaluation of the eyes, Altnel et al. [18] divided them into three groups: failure, partial remission, and complete remission. The thickness of the Ellipsoid Zone (EZ), Outer Nuclear Layer (ONL), and retinal pigment epithelium (RPE) were all assessed using this procedure. In the group of patients with complete remission, the baseline EZ and RPE were discovered to be intact in 71.4% and 64.3% of the eyes, respectively. However, in the failure group, these rates were 25% and 16.7%, respectively. Tang et al. [19] proposed evaluating quantitative indicators associated with treatment response and the beginning of macular neovascularization (MNV) in CSR using an AI-based methodology. In the experiment, eplerenone produced an outstanding reaction in 40/78 (51%) of the eyes, compared to PDT in 38/78 (49%) of the eyes.

## 3. METHODOLOGY

The images collected from a local eye hospital in Cochin, Kerala, India (BWFA dataset) are used to train the classifier (VGG19) used in this research [20]. TL is incorporated to enhance the classifier's performance. In the event of an error, it spreads backwards through the system and modifies the weight of each node.

Iterations of this procedure are repeated over and over, and the distance is continually assessed and improved. Convolutional layers extract the features, and the CNN is trained using these features. A CNN is a DL-based Artificial Neural Network (ANN) architecture. We developed a fairly straightforward method. The convolution layer and max-pooling layer of the CNN, which together form the 2D spatial image (pooling), are mapped to the values in Equations (1) and (2). Every neuron receives an output value z from a function called activation that filters input data $x$ with weight coefficients $w$. If a layer has an $n$ number of neurons, then a specific neuron named $j$ in the following layer gets an $n$ input value. Bias $b_j$ integrates and adds these coefficient-weighted inputs. $w_{i,j}$ is the weight applied to the input of $i^{th}$ neuron to produce an output at $j^{th}$ neuron. A neuron's activation function f produces the signal $z_j$. Fig. 2 shows the structure of an artificial neural network.

$$y_j = b_j + \sum_{i=1}^{n} w_{i,j} x_i \tag{1}$$

$$z_j = f(y_j) \tag{2}$$

The input variable x is assumed to have L x L 2D source pixels and to be processed by convolution with a table of weights using H x H window. After extracting values of the same size from the source image, the convolution combines the weighting factors of the window H x H by the filter values of the pixels for the source. By shifting the window, then the process of filtering is applied once more to the source image. It should be mentioned that a zero-padding method was included to make sure that both the input and output are of the same size.

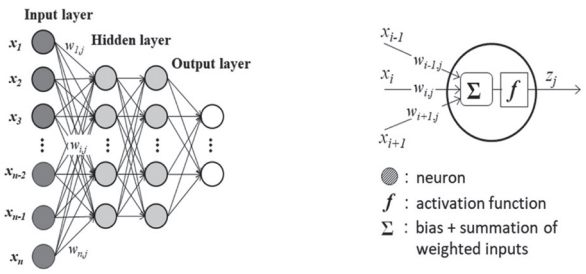


(a) (b)

**Fig. 2.** Structure of ANN (a) Data Flow in DL (b) Inner Structure of Neuron

The convolution operation is displayed in Fig. 3. As $x_{i,j}$ is then multiplied by $w_{k,l,n}$, a grid at (*i,j*) on the filters is independently shifted. This equation is written as follows, incorporating the bias bn in the expression and the convolution form:

$$y_{i,j,n} = \sum_{k=0}^{H-1} \sum_{l=0}^{H-1} w_{k,l,n} x_{i+k,j+1} + b_n \tag{3}$$

$$z_{i,j,n} = f(y_{i,j,n}) \tag{4}$$

$y_{i,j,n}$ represents the convolution output of the image with a weighing filter and $z_{i,j,n}$ is the final output after applying a rectified linear unit (ReLU) as the activation

function (f), which could select positive input values as a result of an improvement in matrix conversion.

$$f(y_{i,j,n}) = \max(y_{i,j,n}, 0) \quad (5)$$

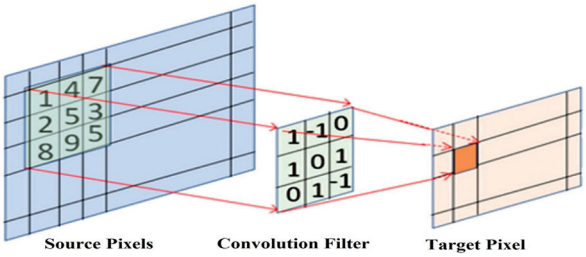


**Fig. 3.** Convolution Layer with Filter

Equation (6) defines pooling, which is generally used to produce 2D data, but does not include weighted coefficients or activation functions. $p$, $q$ is the domain's horizontal and vertical parts, and $Up$, $q$ is the square unit domain with the dimensions R x R.

$$z_{p,q} = \max(x_{i,j}), (i,j) \epsilon U_{p,q} \quad (6)$$

where $z_{p,q}$ represents the max-pooled output of the processed image sub-region $x_{i,j}$, of the whole image $U_{p,q}$. The same purpose as Equations (1) and (2) is served by these processes, which produce relatively small 2D picture data that are subsequently transmitted to a fully linked layer. These 2D picture data are transformed into several number of 1D digital files that offer details about the classification of the original image. The Soft-Max function in Equation (7) transforms outcomes into probabilities in the output layer. It is a normalized exponential function. It evaluates binary categorization.

$$f(y_j) = \frac{e^{y_j}}{\sum_{r=1}^{m} e^{y_r}} \quad (7)$$

$f_{yj}$ represents the softmax function that converts the output score of each neuron $y_j$ to probabilities of being in a class.

This work considers the existence of two distinct domains. Large datasets used to train a model in a specific (source) domain typically require a lot of time before an accurate prediction can be made. When the model is used in a different (target) domain that is unrelated to the source domain, training takes a lot of time. TL is one of the approaches for improving the effectiveness of the prediction in the target domain (e.g., decreasing run time). For the target domain, the TL can repurpose accumulated common knowledge from the source domain. Recently, the CNN combined with a transfer-learning strategy (CNN-TL) is a successful image classification technique. In this work, CNN-TL was used to transform time series data to picture data because our model should be able to forecast time series. CNN was initially carried in the target domain (Fig. 4a). Second, portions of the CNN's hidden layers were modified before being reapplied to the particular domain. Finally, using datasets from the target domain, "the fully connected layer 1" and "the fully connected layer 2" in the deep layers were re-trained (Fig. 4b).

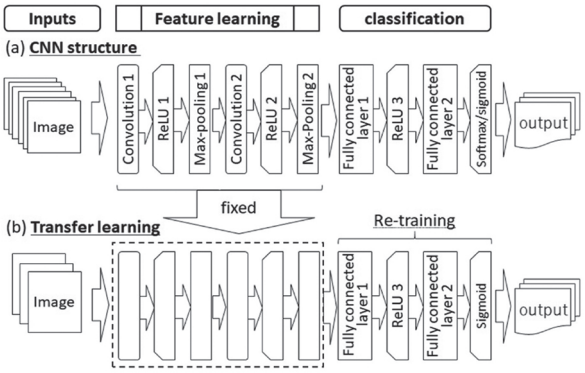


**Fig. 4.** DL Architectures (a) Typical CNN and (b) CNN with TL

The CNN image must match a CSR value for CNN training and prediction operations to be effective. The dataset's images having size 256x256 were chosen because there weren't many variables. As input data, a square image is utilized. A 1x1 of the data output was linked to the data from the input data at the expected time. We assumed that the quantity of the predicted position in the following time step is produced by the CSR data in a square picture. Take note that the predicted point indicates whether or not CSR is present.

## 4. RESULTS AND DISCUSSION

The experimental outcomes of the suggested CSR detection algorithm are shown in this section. Utilizing the BWFA dataset, the proposed TL model's implementation is verified. BWFA images of individuals with CSR disease and BWFA images of healthy people have both undergone classifications. The entire dataset of images was divided into two categories by the algorithm, such as training and testing images. The dataset includes 1600 images from the normal (healthy) group and 1608 images from the CSR category. Sample images from both categories are shown in Fig. 5.

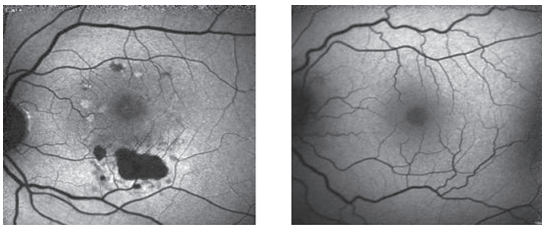

(a) (b)

**Fig. 5.** Sample Images from BWFA Dataset (a) CSR (b) Healthy.

The research addresses the class imbalance problem. The distribution of samples for the training classes is uniform. 70% of the images from each class were taken for training the CNN. The remaining 30% of the images from each class were used for testing the CNN.

Fig. 6 shows the distribution of BWFA images into different groups, which are used for training and testing the classifier.

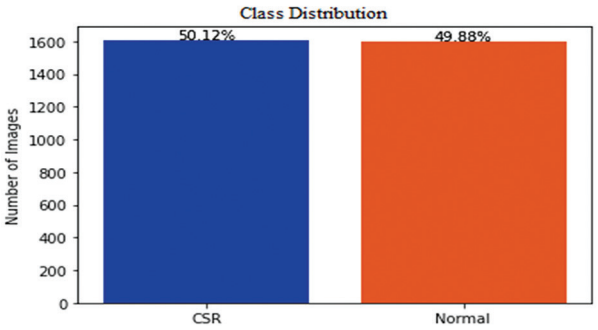


**Fig. 6.** BWFA Dataset Class Distribution

The input to this network has a fixed-size (256 * 256) RGB image. Hence the matrix had the structure of (256, 256, 3). The mean RGB value of each pixel, calculated throughout the whole training set, was the only preprocessing that was carried out. They made use of kernels with a stride size of 3 × 3 pixels. They were able to completely hide the image because of this. Spatial padding is being used to preserve the spatial resolution of the image. Max pooling was done with stride 2 above a 2x2 pixel window. ReLu was then used to add non-linearity, which improved computational efficiency and helped the model better categorise data than earlier models that employed tanh or sigmoid functions.

VGG19 is a CNN having 19 hidden layers in total. It is possible to load a network that has already been trained using more than a million images from the ImageNet database. The pre-trained network can categorize images into more than 1000 different object categories and has amassed rich visual information for a range of images. After loading the pre-trained model and analyzing the feature representations, it is noticed that there are 20,057,153 parameters in total. Of these parameters, 32,769 parameters are trainable. These parameters are trained using the features obtained from the BWFA dataset. The architecture of the proposed modified VGG19 model is depicted in Fig. 7.

The 32,769 parameters are trained using the proposed model by considering binary cross entropy as the loss function. The usage of loss functions is to calculate the quantity that a model should be used to minimize during training. It computes the cross-entropy loss between true labels and predicted labels. Furthermore, when comparing our results to existing work, we used the same settings by using cross-validation and fixed partitioning techniques. The Python language was used to create the pre-trained models based on TL, which were then run on the Google Colab platform [21]. The rate of learning was 1 x 10-4, the minimum batch size was 32 and the optimum epoch count is 50. A reduction in the rate of learning increases the time for the training network while raising it causes training to become locked at an inadequate result [22].

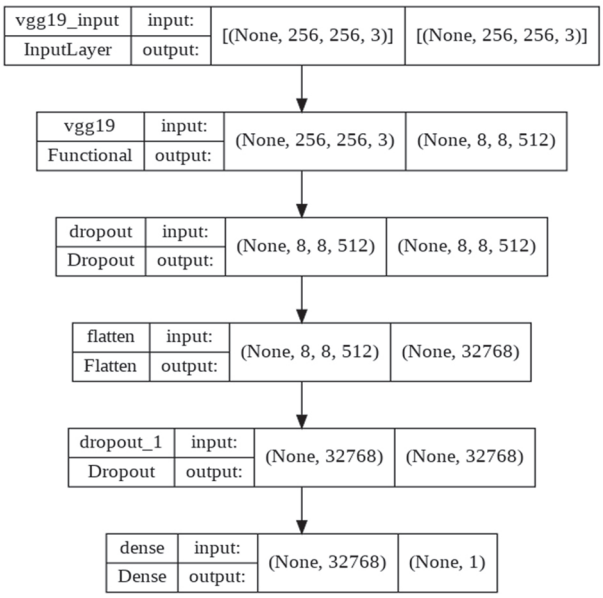


**Fig. 7.** Proposed VGG19 Model Architecture.

Many performance indicators were considered to validate the effectiveness and efficiency of the pre-trained VGG19 model integrating TL. Precision, F1 Score, recall, ROC AUC, specificity, and accuracy are the measures that are most frequently utilized. The words True Positive (TP), False Negative (FN), True Negative (TN), and False Positive (FP) are used to describe classification accuracy. The count of CSR images labelled as CSR is TP and the count of healthy images labelled as healthy is TN. The count of healthy images labelled as CSR is FN and the count of CSR images labelled as healthy is FP [23]. The performance parameters are expressed mathematically as,

$$Precision = \frac{TP}{TP+FP} \tag{8}$$

$$Recall = \frac{TP}{TP+FN} \tag{9}$$

$$F1 = 2 * \frac{Precision*Recall}{Precision+Recall} \tag{10}$$

$$Accuracy = \frac{TN+TP}{TP+FP+TN+FN} \tag{11}$$

$F1$ score is the harmonic mean of precision and recall as indicated in equation 10. Fig. 8 shows the visualization charts for the accuracy of BWFA image classification. The number of iterations (epochs) used in the experiment was 50. The values of performance parameters are stable and high after the 40$^{th}$ epoch. This is due to the classification problem being solved using a TL approach. There is a chance that an error will occur during training, which is referred to as a loss. The proposed VGG19 model with TL for CSR detection has a minimum loss of 0.38, which is quite low as illustrated in Fig. 9. The entire set of test images must be used in the evaluation. The proposed VGG19 with TL model for CSR detection has an average accuracy of 97.30%. Precision and recall have average values of 99.56% and 95.04%, respectively. The proposed model provides an

$F1$ score of 97.25% and a ROC AUC of 97.31%. The maximum number of BWFA images used for training can be increased to increase the classification parameters.


**Fig. 8.** Variation in Accuracy with Epochs

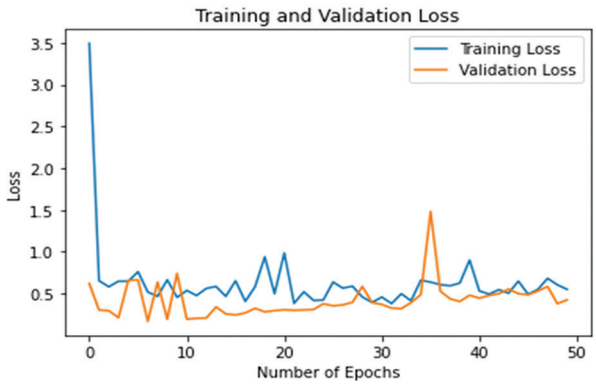


**Fig. 9.** Variation in Loss with Epochs

Experiments have been conducted on the developed model using a given BWFA dataset. The batch size selected for training the model is 32. An experiment is conducted in various steps by varying the number of epochs. The total number of epochs varied from 10 to 50, and the values of performance metrics were computed. 10 epochs provided lower values for the performance parameters, and 50 epochs provided higher values. There was no change in the performance parameters after 50 epochs. So, the experiments are concluded and the values obtained for various performance metrics are given in Table 1. Fig. 10 shows ROC graphs and AUC displays the performance. The overall AUC for this cross-validation research was 0.9731.

**Table 1. Variation in Performance with Epochs**

| Performance Metrics | Epoch | | | | |
|---|---|---|---|---|---|
| | 10 | 20 | 30 | 40 | 50 |
| Accuracy (%) | 95.72 | 96.21 | 97.78 | 96.14 | 97.30 |
| Precision (%) | 94.73 | 96.09 | 96.56 | 98.32 | 99.56 |
| Recall (%) | 92.16 | 91.58 | 93.57 | 93.92 | 95.04 |
| F1 Score (%) | 92.37 | 94.62 | 94.87 | 96.56 | 97.25 |
| Loss | 0.72 | 0.56 | 0.54 | 0.45 | 0.38 |

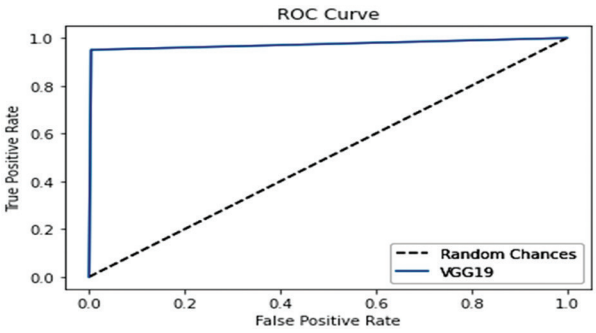


**Fig. 10.** ROC curves for the cross-validation of the proposed model

A detailed comparison of classification performance is required to assess the effectiveness of the proposed TL approach. On various datasets, the proposed transferred models' classification performance is evaluated. Table 2 compares the efficiency of existing models using the selected performance metrics.

**Table 2.** Comparison of CSR Detection Models

| Model | Accuracy (%) | Precision (%) | Recall (%) | F1-Score (%) | Loss (%) |
|---|---|---|---|---|---|
| AlexNet | 95.92 | 96.21 | 94.78 | 92.32 | 0.58 |
| GoogleNet | 88.73 | 89.09 | 86.56 | 90.17 | 0.71 |
| ResNet101 | 92.16 | 91.58 | 90.57 | 91.53 | 0.63 |
| VGG16 | 92.37 | 92.62 | 91.87 | 95.56 | 0.44 |
| Inception v3 | 87.92 | 84.06 | 85.74 | 92.45 | 0.56 |
| Inception ResNet v2 | 89.95 | 89.40 | 91.57 | 93.52 | 0.49 |
| Proposed | 97.30 | 99.56 | 95.04 | 97.25 | 0.38 |

When comparing classification accuracy, the proposed model achieves the best result of 97.30%, which is achieved through TL. In terms of accuracy, pre-trained models like AlexNet (95.92%), ResNet101 (92.16%), and VGG16 (92.37%) performed well. When compared to AlexNet's accuracy, the proposed classification model has an increase of 1.38%. When comparing classification precision, the proposed model achieves 99.56%, which is the highest among all other models. AlexNet's precision was 96.21%, ResNet101's precision was 91.58%, and VGG16's precision was 92.62%. When comparing the proposed classification model to AlexNet's precision, there is a 3.35% increase. The proposed model achieves a recall value of 95.05%. When compared to other models, this has the best recall value. AlexNet had a recall of 95.78%, Inception ResNet v2 had a recall of 91.57%, and VGG16 had a recall of 91.87%. The proposed classification model has a 0.27% increase in recall when compared to AlexNet's recall.

When the training loss is compared, the proposed method and AlexNet have a lower loss. The proposed model has a 0.38 training loss, while the AlexNet model has a 0.58 training loss. When comparing these two models, there is a difference of 0.2. The proposed model achieved the lowest loss and is the best classification

model for CSR detection. The significance of selected parameters demonstrates the value of TL in the reduction of over-fitting and improving classification accuracy. The proposed model and AlexNet were found to be efficient in identifying samples across appropriate datasets. Fig. 11 shows how the performance of the various models compares. In Fig. 12, it is possible to visualise the comparison of training loss.

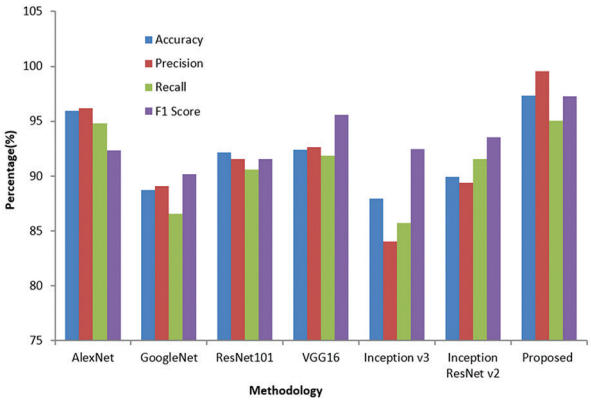


**Fig. 11.** Comparison of Classification Performance

When it comes to CNN-based models, the real motivation comes from the fact that they are used to solve extremely difficult problems using millions of labelled datasets. To create a dataset for DL models, you'll need years of data collection. There are various advantages to employing pre-trained VGG19 systems with TL for categorization. First and foremost, the coding system is automated. Secondly, noise filtering, ROI delineation, feature extraction, and selection are not required anymore. Thirdly, there are no biases, and the pre-trained CNN models' predictions are repeatable. Finally, in contrast to previous CNN-based studies, a ceiling level of accuracy is obtained. The computation time is reduced because we used the Colab platform's CPU and GPU as hardware resources.

## 5. CONCLUSION

In this work, we evaluated various pre-trained CNN techniques employing TL for BWFA image categorization. To get the highest recognition rate, pre-trained CNN methods have been successfully combined with TL. The suggested model surpassed every other model that was put to the test, scoring 97.30% accuracy, 99.56% precision, an F1 score of 97.25% and 95.04% recall for the BWFA datasets. This model uses TL to obtain the lowest training loss of 0.38. The results performed better on CSR classification from BWFA images than current classical and DL techniques. It performs better than current methods in eliminating the requirement for pre-processing procedures. Additionally, compared to existing DL-based work, the pre-trained AlexNet model produces better performance metrics. Future studies will concentrate on putting the models into platforms, reducing computational complexity, and investigating additional methods of fine-tuning.

## 6. REFERENCES:


[1] D. Lu et al. "Deep-learning based multiclass retinal fluid segmentation and detection in optical coherence tomography images using a fully convolutional neural network", Medical Image Analysis, Vol. 54, 2019, pp. 100-110.

[2] J. De Moura, J. Novo, S. Penas, M. Ortega, J. Silva, A. M. Mendonca, "Automatic characterization of the serous retinal detachment associated with the subretinal fluid presence in optical coherence tomography images", Procedia Computer Science, Vol. 126, 2018, pp. 244-253.

[3] H. S. Sandhu et al. "Automated diagnosis of diabetic retinopathy using clinical biomarkers, optical coherence tomography, and optical coherence tomography angiography", American Journal of Ophthalmology, Vol. 216, 2020, pp. 201-206.

[4] A. Miere et al. "Deep learning-based classification of retinal atrophy using fundus autofluorescence imaging", Computers in Biology and Medicine, Vol. 130, 2021, p. 104198.

[5] H. Ullah, M. Faran, Z. Batool, A. Nazir, G. Gilanie, N. Amin, "Diagnosis of Ocular Diseases Using Optical Coherence Tomography (OCT) at λ= 840 nm", Lasers in Engineering (Old City Publishing), 2022, pp. 53.

[6] M. E. Dursun et al. "Evaluation of parafoveal vascular density using optical coherence tomography angiography in patients with central serous chorioretinopathy", Lasers in Medical Science, Vol. 37, No. 2, 2022, pp. 1147-1154.

[7] S. J. Pawan et al. "Capsule Network–based architectures for the segmentation of sub-retinal serous fluid in optical coherence tomography images of central serous chorioretinopathy", Medical & Biological Engineering & Computing, Vol. 59, No. 6, 2021, pp. 1245-1259.

[8] F. Sulzbacher, C. Schütze, M. Burgmüller, P. V. Vécsei-Marlovits, B. Weingessel, "Clinical evaluation of neovascular and non-neovascular chronic central serous chorioretinopathy (CSC) diagnosed by swept-source optical coherence tomography angiography (SS OCTA)", Graefe's Archive for Clinical and Experimental Ophthalmology, Vol. 257, No. 8, 2019, pp. 1581-1590.

[9] E. Borrelli et al. "Optical coherence tomography parameters as predictors of treatment response to eplerenone in central serous chorioretinopathy", Journal of Clinical Medicine, Vol. 8, No. 9, 2019, p. 1271.

[10] K. Aggarwal et al. "Distinguishing features of acute Vogt-Koyanagi-Harada disease and acute central serous chorioretinopathy on optical coherence tomography angiography and en face optical coherence tomography imaging", Journal of Ophthalmic inflammation and infection, Vol. 7, No. 1, 2017, pp. 1-9.

[11] S. Sonoda et al. "Structural changes of inner and outer choroid in central serous chorioretinopathy determined by optical coherence tomography", PLoS One, Vol. 11, No. 6, 2016, p. e0157190.

[12] A. N. Kulikov, E. Y. Malahova, D. S. Maltsev, "Artificial intelligence and machine learning for optical coherence tomography-based diagnosis in central serous chorioretinopathy", Ophthalmology Journal, Vol. 12, No. 1, 2019, pp. 13-20.

[13] J. Yoon et al. "Optical coherence tomography-based deep-learning model for detecting central serous chorioretinopathy", Scientific Reports, Vol. 10, No. 1, 2020, pp. 1-9.

[14] D. Jaisankar, M. Kumar, P. Rishi, S. Singh, R. Raman, "Correlation of retinal changes with choroidal changes in acute and recurrent central serous chorioretinopathy assessed by swept-source optical coherence tomography", Therapeutic Advances in Ophthalmology, Vol. 12, 2020, p. 2515841419899823.

[15] S. Khalid, M. U. Akram, T. Hassan, A. Nasim, A. Jameel, "Fully automated robust system to detect retinal edema, central serous chorioretinopathy, and age-related macular degeneration from optical coherence tomography images", BioMed Research International, 2017.

[16] W. J. Lee, J. W. Lee, S. H. Park, B. R. Lee, "En-face choroidal vascular feature imaging in acute and chronic central serous chorioretinopathy using swept source optical coherence tomography", British Journal of Ophthalmology, Vol. 101, No. 5, 2017, pp. 580-586.

[17] J. Yang, E. Wang, M. Yuan, Y. Chen, "Three-dimensional choroidal vascularity index in acute central serous chorioretinopathy using swept-source optical coherence tomography", Graefe's Archive for Clinical and Experimental Ophthalmology, Vol. 258, No. 2, 2020, pp. 241-247.

[18] M. G. Altınel, B. Acikalin, H. Gunes, G. Demir, "Optical coherence tomography parameters as predictors of treatment response to a 577-nm subthreshold micropulse laser in chronic central serous chorioretinopathy", Lasers in Medical Science, Vol. 36, No. 7, 2021, pp. 1505-1514.

[19] A. A. Tang, A. L. Lin, "Purtscher-like retinopathy in adult-onset Still's disease, complicated by treatment-related central serous chorioretinopathy", American Journal of Ophthalmology Case Reports, Vol. 18, 2020, p. 100631.

[20] P. Gholami, P. Roy, M. K. Parthasarathy, V. Lakshminarayanan, "OCTID: Optical coherence tomography image database", Computers & Electrical Engineering, Vol. 81, 2020, p. 106532.

[21] T. Sekiryu, "Choroidal imaging using optical coherence tomography: techniques and interpretations", Japanese Journal of Ophthalmology, 2022, pp. 1-14.

[22] K. Gao et al. "Double-branched and area-constraint fully convolutional networks for automated serous retinal detachment segmentation in SD-OCT images", Computer methods and programs in biomedicine, Vol. 176, 2019, pp. 69-80.

[23] S. S. Mishra, B. Mandal, N. B. Puhan, "Macular Net: Towards Fully Automated Attention-Based Deep CNN for Macular Disease Classification", SN Computer Science, Vol. 3, No. 2, 2022, pp. 1-16.

[24] M. Treder, J. L. Lauermann, N. Eter, "Deep learning-based detection and classification of geographic atrophy using a deep convolutional neural network classifier", Graefe's Archive for Clinical and Experimental Ophthalmology, Vol. 256, No. 11, 2018, pp. 2053-2060.

[25] R. Narendra, G. N. Girish, A. R. Kothari, J. Rajan, "Deep Learning Based Sub-Retinal Fluid Segmentation in Central Serous Chorioretinopathy Optical Coherence Tomography Scans", Proceedings of the 41st Annual International Conference of the IEEE Engineering in Medicine and Biology Society, pp. 978–981.